

RESEARCH ARTICLE

10.1002/2014JB011372

Key Points:

- Energy-dependent joint tomography at the erupting Mount St. Helens volcano
- Tomographic model of its 6–18 km deep tectonic and feeding systems
- Overcoming ray-dependent tomography in volcanoes

Supporting Information:

- Readme
- Text S1
- Figure S1
- Figure S2
- Figure S3
- Figure S4

Correspondence to:

L. De Siena,
lucadesiena@uni-muenster.de

Citation:

De Siena, L., C. Thomas, G. P. Waite, S. C. Moran, and S. Klemme (2014), Attenuation and scattering tomography of the deep plumbing system of Mount St. Helens, *J. Geophys. Res. Solid Earth*, 119, doi:10.1002/2014JB011372.

Received 12 JUN 2014

Accepted 13 OCT 2014

Accepted article online 20 OCT 2014

Attenuation and scattering tomography of the deep plumbing system of Mount St. Helens

L. De Siena^{1,2}, C. Thomas¹, G. P. Waite³, S. C. Moran⁴, and S. Klemme⁵

¹Institut für Geophysik, University of Münster, Münster, Germany, ²Department of Geology and Petroleum Geology, School of Geosciences, University of Aberdeen, Aberdeen, UK, ³Department of Geological Engineering and Sciences, Michigan Technological University, Houghton, Michigan, USA, ⁴U.S. Geological Survey, Vancouver, Washington, USA, ⁵Institut für Mineralogie, University of Münster, Münster, Germany

Abstract We present a combined 3-D *P* wave attenuation, 2-D *S* coda attenuation, and 3-D *S* coda scattering tomography model of fluid pathways, feeding systems, and sediments below Mount St. Helens (MSH) volcano between depths of 0 and 18 km. High-scattering and high-attenuation shallow anomalies are indicative of magma and fluid-rich zones within and below the volcanic edifice down to 6 km depth, where a high-scattering body outlines the top of deeper aseismic velocity anomalies. Both the volcanic edifice and these structures induce a combination of strong scattering and attenuation on any seismic wavefield, particularly those recorded on the northern and eastern flanks of the volcanic cone. North of the cone between depths of 0 and 10 km, a low-velocity, high-scattering, and high-attenuation north-south trending trough is attributed to thick piles of Tertiary marine sediments within the St. Helens Seismic Zone. A laterally extended 3-D scattering contrast at depths of 10 to 14 km is related to the boundary between upper and lower crust and caused in our interpretation by the large-scale interaction of the Siletz terrane with the Cascade arc crust. This contrast presents a low-scattering, 4–6 km² “hole” under the northeastern flank of the volcano. We infer that this section represents the main path of magma ascent from depths greater than 6 km at MSH, with a small north-east shift in the lower plumbing system of the volcano. We conclude that combinations of different nonstandard tomographic methods, leading toward full-waveform tomography, represent the future of seismic volcano imaging.

1. Introduction

Mount St. Helens (MSH) is one of the most active volcanoes in the United States. Both its spectacular May 1980 eruption and its most recent 2004–2008 dome-building eruption are among the best studied examples of subduction-related dacite eruptions [Sherrod *et al.*, 2008]. However, our understanding of how the deep plumbing system works is still poorly constrained.

The most recent *P* wave velocity model of MSH [Waite and Moran, 2009] integrates travel time data used by previous velocity tomography studies at regional and local scales [Lees and Crosson, 1989; Lees, 1992; Moran *et al.*, 1999] with the ones produced during the last eruption cycle. Waite and Moran [2009] show a volcanic edifice which appears as a low-velocity anomaly for *P* waves. They also provide high-resolution images of the upper plumbing system, located under the cone, and separated in their interpretation in an upper (depths of 1 to 3 km, Figure 1) and a lower (deeper than 6 km, Figure 1) magmatic chamber, interspersed with several high-velocity structures [Waite and Moran, 2009]. In the same volumes, Lees [1992] shows that a low-velocity anomaly, extending between depths of 3.5 and 6 km, lies at the top of a unique high-velocity anomaly (6–9 km deep). This high-velocity anomaly is interpreted as a plug of solidified material, which lies at the top of the 9 km deep magma chamber. In Figure 1, we propose a simplified sketch of the main tomographic results and interpretations provided by scientists after its 1980 eruption.

At depths greater than 6 km, travel time tomography does not provide high-resolution images under the volcanic edifice. In the regions surrounding the volcanic edifice, however, regional-scale tomography shows a persistent *P* wave low-velocity north-south trending anomaly between depths of 0 and 10 km [Lees and Crosson, 1989; Moran *et al.*, 1999], located between Mount Rainier and MSH, approximately following the so-called St. Helens Seismic Zone (SHZ). Moran *et al.* [1999] interpret this feature as due to the presence of Tertiary marine sediments preserved in the cracked volumes surrounding the SHZ.

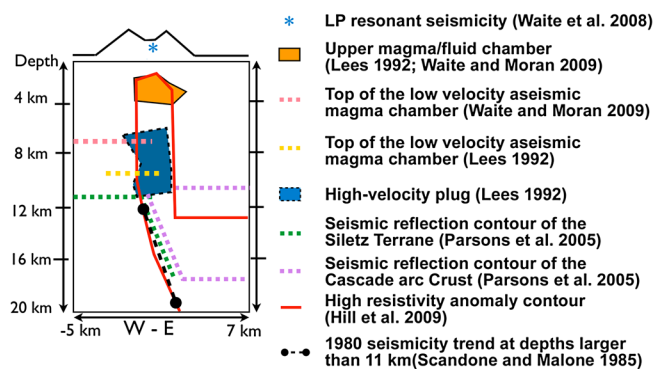


Figure 1. A simplified sketch of the main tomography results (and corresponding interpretations) obtained under the MSH volcanic edifice by means of different geophysical techniques. The references are cited in the text and discussed in section 1.

slip consistent with magma being periodically injected into a truncated dike on the northwest side of this fault.

P and coda wave attenuation studies that used seismicity recorded during the 1980–1986 and 1996–1998 seismic swarms showed that temporal changes and an increased complexity with depth affect seismic observations sampling the cone and the volumes underneath [Fehler *et al.*, 1988; Tusa *et al.*, 2004]. The temporal changes may reflect changes in the upper feeding system of the volcano, as suggested by the petrological studies of Pallister *et al.* [2008]. These authors compare new petrological data obtained during the 2004–2008 eruptive cycle with fluid/melt inclusions sampled from rocks related either to the 1980–1986 or to the Goat Rocks (A.D. 1800–1857) eruptive cycles. They suggest the ascent of a geochemically distinct batch of magma into the apex of the magma reservoir during the period 1987–1997, followed by upward movement of magma beginning in late September 2004 [Pallister *et al.*, 1992, 2008]. Seismic data, however, generally show that the 2004–2008 eruption conduit is approximately in the same place as the one that fed the 1980 eruption.

The most recent eruptive activity produced a large number of repetitive long-period (LP, Figure 1) and very long period earthquakes related to the resonance of a gently NNW-dipping, steam-filled crack and to the compression and expansion of a shallow, magma-filled sill, respectively [Sherrod *et al.*, 2008; Waite *et al.*, 2008]. These events were accompanied by smaller near-continuous events that occurred randomly until 2006 [Matoza and Chouet, 2010]. By the application of waveform correlation techniques to the recordings of these sources, Matoza and Chouet [2010] infer an interaction between the uppermost conduit and the shallow hydrothermal system, which may have had a critical role in the 8 March 2005 phreatic explosion and during the entire eruption period.

A high-resistivity vertical anomaly, shifted east of the central cone and interpreted as a continuous path for magma ascent (Figure 1), has been obtained by a recent application of magnetotelluric tomography [Hill *et al.*, 2009]. Between depths of 10 and 15 km this conductive anomaly ends in a thick midcrustal conductor extending to the east. In the interpretation of Hill *et al.* [2009], also based on the 1980 deep seismicity following its western contour, the deeper anomaly is an image of the Southern Washington Cascades Conductor [Egbert and Booker, 1993] and is comprised of interconnected melt fraction (Figure 1).

A 530 km long wide-angle onshore-offshore seismic transect across the Cascadia subduction zone was recorded to study the major structures that contribute to seismogenic deformation. Parsons *et al.* [2005] observe a distinct transition from Siletz terrane into Cascade arc crust that coincides with the SHZ at MSH (Figure 1). The boundary between these two structures dips slightly eastward and supports the idea that the mafic Siletz terrane focuses seismic deformation at its edges [Parsons *et al.*, 2005]. From the measured crustal structure and subduction geometry, Parsons *et al.* [2005] identify a crustal zone at the eastern boundary between the Siletz terrane and the Cascade Range that may concentrate future seismic activity. The seismicity below 11 km recorded at MSH during the 1980–1986 eruptive cycle follows a similar trend (Figure 1).

The study of the seismicity recorded at MSH both during the 1980–1986 eruptive cycle [Scandone and Malone, 1985] and the 1996–1998 seismic swarms [Musumeci *et al.*, 2002; Tusa *et al.*, 2004] suggests a feeding model in which magma is supplied from depths of 5.5 to 10 km, connected to the surface by a thin vertical conduit. Musumeci *et al.* [2002] show how some of the deeper events occur along a sequence of faults under the influence of a radial stress field. They comment that a large number of the events occur on a NNE-SSW striking, steeply dipping fault with

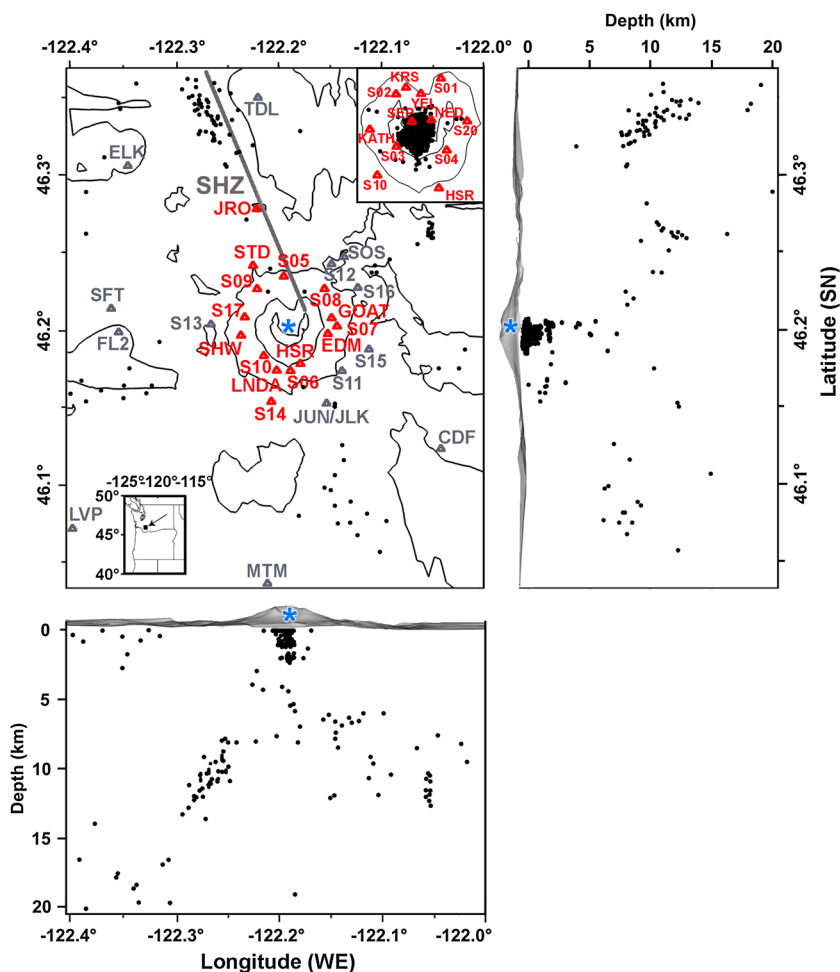


Figure 2. The temporary broadband stations and a subset of the permanent network stations displayed on topography contoured at 500 m intervals. Inset in the lower left and upper right corners show the location of Mount St. Helens in southern Washington and a close-up of the crater, respectively. The St. Helens Seismic Zone (SHZ) is plotted following the seismicity recorded in the period 2000–2006 (black dots). The blue star corresponds to the approximate location of resonant long-period events with a dominant frequency of 1.7 Hz [Waite *et al.*, 2008] acting during the eruption. At the red stations we record higher coda energies and higher direct attenuation than at grey stations.

When targeting volcanic structures, scattering heavily affects any tomographic result, corrupting direct phases and/or amplitudes and rapidly producing incoherent signals [Wegler and Lühr, 2001; Sato *et al.*, 2012]. Due to insufficient ray crossing in regions of low seismicity, we can only obtain sufficiently resolved *P* wave attenuation images (where attenuation is measured by the *P* wave quality factor) in the cone and in the volumes surrounding the main fault systems, where the seismicity is concentrated (Figure 2). These are also the regions of highest heterogeneity, where coherence is quickly lost.

Direct wave total attenuation adds information on the amount of energy dissipated into the medium due to scattering and intrinsic mechanisms [Sato *et al.*, 2012]. The scattered wavefield, primarily composed of *S* waves and recorded as the tail portion of the waveform in a high-frequency seismogram, can be modeled by single and multiple scattering in the crust, mantle, and core [Margerin and Nolet, 2003; Sato *et al.*, 2012]. The coda normalization method [Aki, 1980; Yoshimoto *et al.*, 1993] measures the total direct quality factor, *Q*, which is related to the scattering (*Q_s*) and the intrinsic (*Q_i*) quality factors by the simple linear relationship: $Q^{-1} = Q_s^{-1} + Q_i^{-1}$ [Sato *et al.*, 2012, chapter 2]. In recent years the coda normalization method, which removes the influence of site, source intensity, and instrument response from the data, has been extended to direct wave attenuation tomography and applied to both volcanic cones and calderas [Del Pezzo *et al.*, 2006; De Siena *et al.*, 2010, 2014].

At both MSH and Mount Vesuvius, the study of either the average P or S wave direct attenuation with the coda normalization method shows large frequency-dependent differences in total attenuation when using near-volcano and far-volcano earthquakes [De Siena *et al.*, 2014]. Similar results are obtained by the separation of Q_s and Q_p at Mount Fuji. Chung *et al.* [2009] show that both values in the near-Fuji area are greater than those of the far-Fuji area. In both cases, the results are interpreted in terms of higher lithospheric heterogeneity in the volcanic edifice and feeding system.

S scattered waves can be used as the main source of information to reconstruct deep structures in the entire medium, especially if melt and/or fluids are present [Asano *et al.*, 2004]. Smaller direct and coda amplitudes characterize waveforms crossing melt and fluid reservoirs, while a volcanic cone acts as a strong scatterer, increasing incoherent coda amplitudes or creating surface waves [Wegler, 2003; Asano *et al.*, 2004; Parsiegla and Wegler, 2008; Yamamoto and Sato, 2010; Sato *et al.*, 2012]. S wave coda intensities may therefore provide the 3-D location and scattering power of highly scattering bodies in a 3-D tomographic approach, where the scattering power is measured by using the scattering coefficient, g [Nishigami, 1991, 2006; Tramelli *et al.*, 2006]. Such a powerful technique is apt to distinguish highly scattering bodies (as melt, fluid, and sediments) and seismic interfaces in the depth range where scattered waves propagate [Asano and Hasegawa, 2004; Nishigami, 2000; Tramelli *et al.*, 2006]. Although the interpretation of scattering anomalies (either positive or negative deflections of the energy envelope) is challenging [Calvet and Margerin, 2013; Mayor *et al.*, 2014], the combined use of scattering and attenuation tomography may produce images of the magma and fluid pathways under the volcano, between depths of 0 and 18 km.

2. Data and Methods

2.1. Data

The seismic waveforms used in this study were recorded using 39 seismic stations, running from 2000 to 2006, before and during the last eruption of MSH in 2004–2008. These stations can be divided in two categories: the Pacific Northwest Seismic Network permanent network (mostly short-period vertical sensors), and two temporary arrays of three-component broadband stations located directly on or in proximity of the cone ([Sherrod *et al.*, 2008; Waite and Moran, 2009], see also the Incorporated Research Institutions for Seismology Data Management Center internet site). We select a total of 5534 velocity recordings produced from 540 earthquakes having usable coda, with usable coda defined as events having more than 1.5 times signal to noise at lapse times larger than 50 s, and deconvolve the instrument response.

We do not use absolute amplitude information to obtain exact measurements of direct attenuation (Q) and scattering (g): we simply obtain variations of these two parameters with respect to an average. The exponential decrease of the coda envelopes, the energy ratios, and, more generally, the shape of the envelopes in the considered time windows (see supporting information (SI)) are similar if we use either the two horizontal or the vertical components, as shown by both Musumeci *et al.* [2002] and Waite *et al.* [2008]. As this is true for different source types, we assume that the high-scattering characteristics of the heterogeneous volcano are sufficient to justify the use of vertical sensors for our application, even if those are mainly composed of S waves [Sato *et al.*, 2012, chapter 2.4.1]. We consider the use of an approximated S wave velocity model to be a more important shortcoming of our method (SI).

We exclude from the analysis earthquakes with a small difference in S -minus- P arrival. If this difference is too short, we cannot provide stable P wave energy measurements. Ray lengths are obtained by using a ray-bending approach [Block, 1991] in the most up-to-date P wave velocity model for this region [Waite and Moran, 2009]. We exploit the characteristics of the seismicity during the time of active magma extrusion using a repeated long-period (LP) source of known magnitude and radiation pattern located inside the volcanic cone (Figure 2, blue star). The 2367 recordings of the LP source at different stations sample the shallower part of the region shown in Figure 2.

Coda energies are calculated starting at 15 s from the nucleation time with a moving time window approach, after filtering in the 6 Hz frequency band (passband filter between 4 and 8 Hz). The moving window duration is set to 2 s, following the resolution criteria outlined in, e.g., Tramelli *et al.* [2006]. Direct P wave energy is measured on the same traces using a fixed window of 1 s in order to avoid contamination with the direct S wave. We calculate the energy density of the direct and coda waves as the sum of the squared filtered time trace and of its Hilbert transform [Wegler and Lühr, 2001; Tramelli *et al.*, 2009].

2.2. Q_c Mapping and 2-D Spatially Dependent Behavior of Direct and Coda Phases

Coda and direct waves are sensitive to the variable anelasticity and elastic heterogeneity of the medium. These variations affect observations of the integral over time of the coda energies (from now on named “coda energies”) as well as of the P -to-coda spectral ratios, which are the quantities inverted in the 3-D scattering and attenuation tomographies. At MSH the largest perturbations, causing strong amplitude variations and P wave attenuation (see Figures S1 and S2 in the supporting information), affect the waves crossing the cone and the southern part of the SHZ (i.e., the red stations in Figure 2, see also *De Siena et al.* [2014]).

We do not know if these regions also cause strong Q_c variations. Hence, coda amplitude time decays are used to provide a 2-D map of the structures which produce the largest attenuation of scattered waves by adopting the regionalization approach for the S wave coda quality factor [*Sato et al.*, 2012; *Calvet et al.*, 2013]. In the 4–8 Hz frequency band we follow the regionalization approach described by *Calvet et al.* [2013].

For each trace we model the coda energy density $E(t, f)$ at lapse time from the origin time of the event (t) and frequency (f) with the following equation:

$$E(t, f) = S(f)t^{-1.5} \exp\left(-\frac{2\pi ft}{Q_c(f)}\right) \quad (1)$$

after *Aki and Chouet* [1975], interpreting the coda with the diffusion approximation, where $S(f)$ is the frequency-dependent source term. After dividing the energy density by the average source intensity in the 6 Hz frequency band, we map the Q_c spatial distribution allocating the mean values of the Q_c to each block in a 2-D grid of 2 km size, crossed by a minimum of two raypaths.

Calvet and Margerin [2013] highlight the importance of carefully selecting time windows in the coda to avoid bias introduced by the transient regime. We chose a 30 s time window beginning 15 s after the earthquake origin time. Since a large part of the seismicity is concentrated in or just below the cone, such a long lapse time will affect the resolution of the 3-D scattering tomography in this region, as described in the next sections. We remark that strong coda wave attenuation is concentrated under the volcanic cone and, less obviously, along the SHZ trend (Figure 3, $\alpha - \delta$), while the rest of the medium is uniform in comparison.

We compare this 2-D map with several seismograms from a single LP source in the cone (Figure 3, blue star) and recorded at the same ray distances (between 6 and 7 km in Figure 3, see also the SI Figures S3 and S4). In order to have a quantitative measurement for each seismogram, we define the rise time, t_r , as the time between the first onset (P arrival) of the envelope and its maximum as well as the maximum amplitude of the seismogram (a_m , measured in mm/s). These values are shown above each seismogram in blue if the maximum corresponds to a visible S wave arrival, in red otherwise. The seismograms all show clear P wave arrivals, while the S wave arrival is often hardly discernible from the P wave coda.

The lateral extensions of the high coda attenuation body in the northern and eastern directions are clearly connected with the energy decrease of the S wave direct phase, the corresponding amplitude increase of coda coherent-like phases, and a general decrease in maximum amplitudes in the seismograms. Approximately at the same ray distance the seismograms recorded north and east of the source are characterized by a delayed maximum of the envelope, which produces a much larger rise time (red, Figure 3). The lower maximum amplitudes at these sites (a_m , red, north and east of the source) reflect a second coherent-like phase, produced by the interaction with the complex medium after a few mean free paths from the source [*Sato et al.*, 2012; *De Siena et al.*, 2013]. The direct S waves, whose amplitudes are strongly attenuated if propagating north and east of the cone, generally produce the maximum amplitudes if recorded south and south-west of the source (blue, Figure 3).

The comparison of the 2-D Q_c map with unfiltered seismograms shows that the simple 2-D map is correlated with complex observations: near to the red anomalies, direct S waves disappear, scattered phases become stronger, and amplitudes decrease. Nevertheless, the 2-D mapping may not account for the complexities at all hypocentral distances (SI). Hence, 3-D scattering and coda normalization tomographies are necessary for generating more complex 3-D models of coda variations at MSH. We do not interpret all the anomalies in Figure 3 or test the fine-scale resolution of this image, as we do for the other two tomographies. There is large indetermination in the physical meaning of Q_c , a quantity which is strongly dependent on lapse time and frequency and deserves a separate study [*Calvet and Margerin*, 2013].

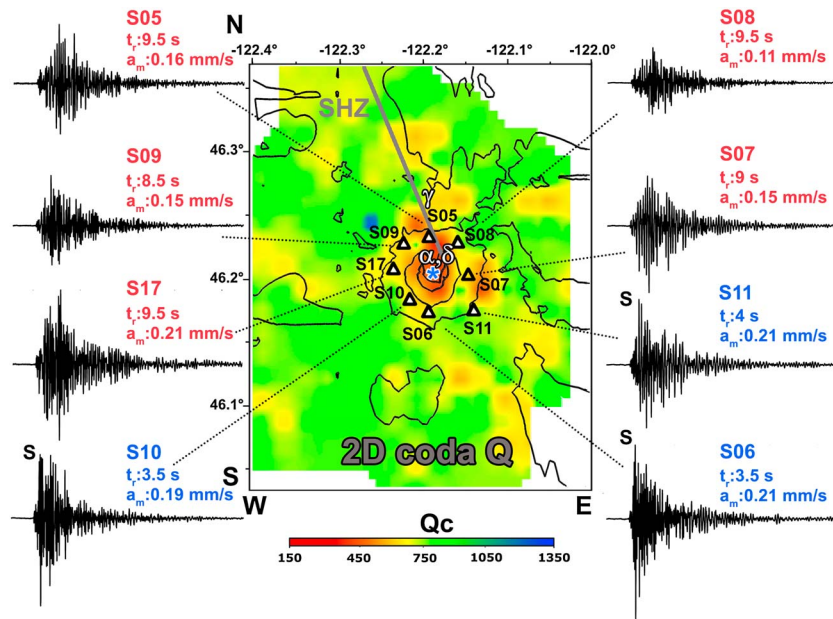


Figure 3. The colored map shows the result of the 2-D Q_c tomography. The blue star shows the location of a long-period source inside the cone (nucleation time on the 29 June 2005 at 07:00:56). The unfiltered recordings (each of duration 45 s) of the earthquake at eight stations (triangles) are shown on the left and right side of the map, connected to the corresponding station by a dotted black line, after deconvolution for the instrument response. The ray lengths corresponding to the recordings vary between 6 and 7 km. The rise time and the maximum amplitude of the envelope (t_r and a_m , respectively) are written in blue if a visible S direct wave produces the maximum of the envelopes, in red otherwise. White-faced bold Greek letters label the regions discussed in the text.

2.3. Scattering and Total Attenuation 3-D Tomography

In the following text we briefly describe the methods which have been applied to obtain the attenuation [De Siena et al., 2014] and scattering [Tramelli et al., 2006] images. We invite the reader to examine the SI, section S3, where we discuss our inversion procedures in detail. There we particularly focus on the existence of a forward model for the scattering tomography as well as on both the limits and the stability of the results of the two inversions.

2.3.1. Three-Dimensional Scattering Tomography

Scattering tomography assumes that, in a volume with average scattering power, the strongest scatterers can be approximated as single-scattering regions, producing strong changes in coda envelopes at different lapse times [Nishigami, 1991; Matsumoto et al., 1998; Asano and Hasegawa, 2004; Nishigami, 2000; Tramelli et al., 2006, 2009]. The scattering power of the blocks constituting a 3-D grid is related in the inversion problem to the ratio between the energy recorded in a 2 s coda time window, ϵ_n , and corresponding to the location of the n th inhomogeneity (over a total of N) and the average homogeneous energy, ϵ (both integrated over time), ϵ_n/ϵ :

$$\frac{\epsilon_n}{\epsilon} = \frac{\sum_{i=1}^N (\alpha_i / r_{ai}^2 r_{bi}^2)}{\sum_{i=1}^N (1 / r_{ai}^2 r_{bi}^2)} \quad (2)$$

where r_{ai} and r_{bi} are the distances of the inhomogeneity from the source and the receiver, respectively.

The method does not rely on direct phase propagation and is able to image the main scatterers in a highly heterogeneous environment, that is, the zones producing energy in the recorded wavefield as lapse time from nucleation increases. The scattering power (α_i) or scattering coefficient (g_i (km^{-1}), equal to the inverse mean free path) are inferred from measurement of the intensity recorded in the scattered wavefield (coda waves) as a function of lapse time and frequency.

As in Tramelli et al. [2009], we assume that the strongest scatterers in a complex heterogeneous medium will produce intensity increases which may be modeled by assuming single scattering. In other words, we extract single-scattering components in a diffusion dominant process. The linear inversion of equation (2) with respect to an average envelope, computed for the entire region under study, provides tomographic

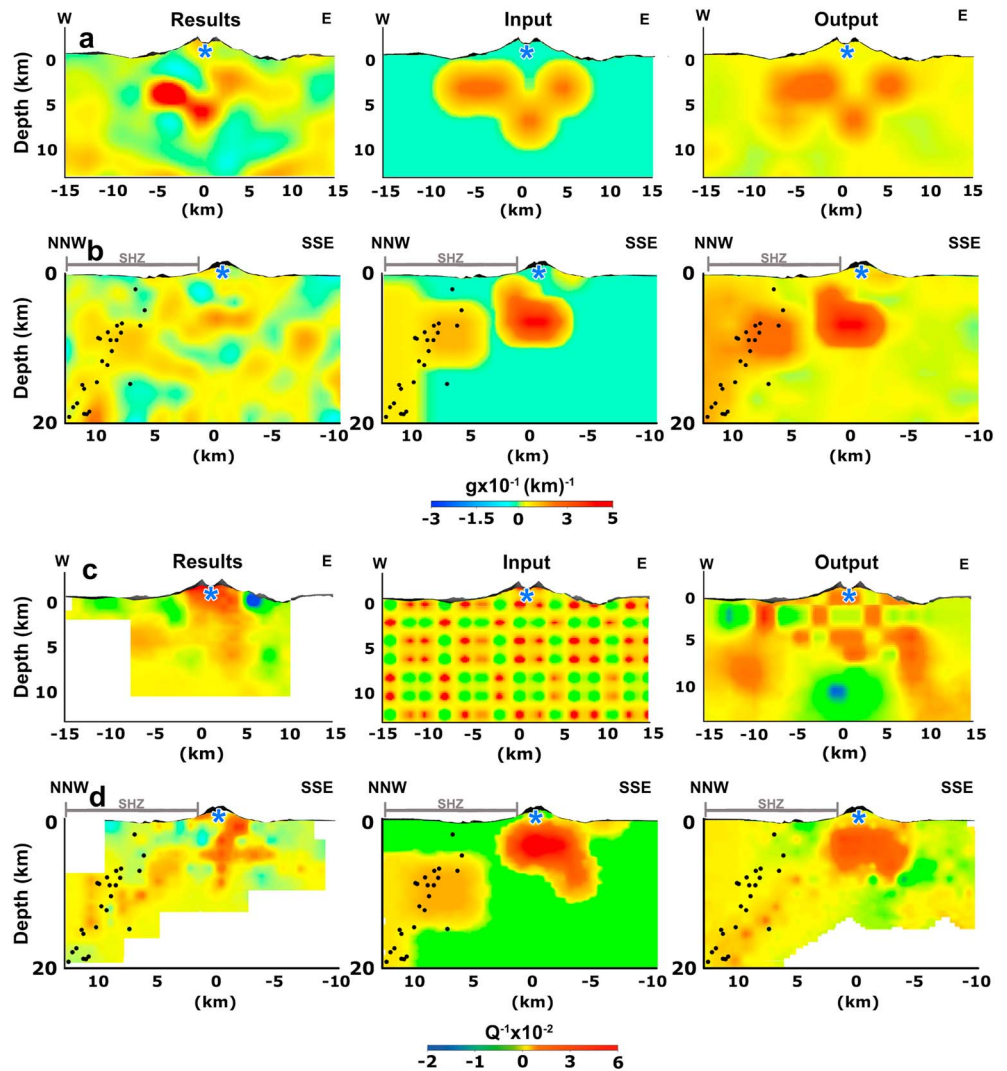


Figure 4. (a) The results of (left) the scattering tomography as well as (middle) the input and (right) output of the corresponding reconstruction test are shown on a vertical slice crossing the volumes under the central cone. (b) The scattering structure and the corresponding reconstruction test are shown on a vertical slice approximately following the SHZ. (c) The results of (left) the attenuation tomography as well as (middle) the input and (right) output of the corresponding synthetic checkerboard structure, having variable node spacing (2 km or 4 km), are shown on a vertical slice crossing the volumes under the central cone. (d) The total attenuation structure and the corresponding reconstruction test are shown on a vertical slice approximately following the SHZ. The seismicity of the period 2000–2006 following the SHZ is imposed in Figures 4b and 4d.

images of the lateral and depth variations of the scattered wavefield; that is, the technique locates the main scatterers in the volume under study [Tramelli et al., 2006, 2009].

2.3.2. Three-Dimensional P Wave Attenuation Tomography With the Coda Normalization Method

The coda normalization method, first developed to obtain average P and S wave attenuation at a regional scale, mixes direct and coda information and has been used to image the attenuation structures of volcanoes at regional and local scales [Yoshimoto et al., 1993; Del Pezzo et al., 2006; Sato et al., 2012; De Siena et al., 2014]. The result is strictly dependent on the relative effect of scattering on direct and coda waves. The data in the inversion problem are given by the logarithm of the energy ratio between the P direct energy (computed on a time window of 1 s) and the S coda energy, multiplied for the inverse geometrical spreading ($E_p r^{\gamma} / E_c$):

$$\frac{E_p r^{\gamma}}{E_c} = \log(G(f, t)) - 2\pi f \sum_{\text{ray}} \frac{dl}{v(l)Q(l)} \tag{3}$$

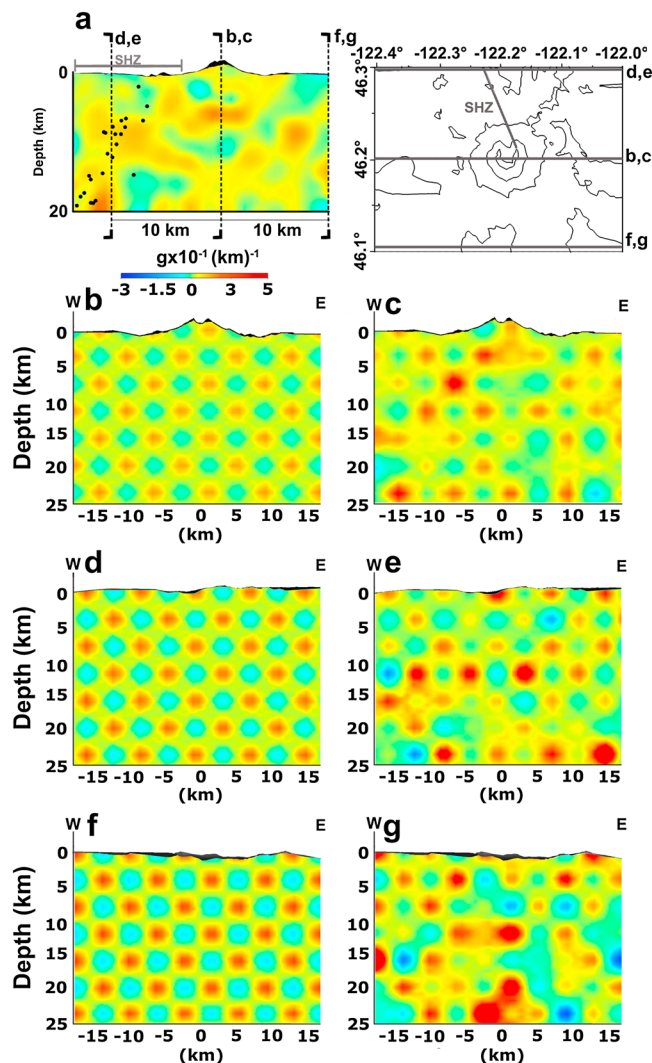


Figure 5. (a) The results of (left) the scattering tomography are shown on a vertical profile along the direction of the SHZ, together with the 2000–2006 seismicity (black dots) along the SHZ. The inputs and outputs of a checkerboard test with 4 km node spacing are reproduced on vertical WE slices, crossing (b, c) the cone and the volumes (d, e) 10 km north and (f, g) 10 km south of it. (right) We also show on a map (Figure 5a) the location of the vertical slices reproduced in Figures 5b–5g.

radiation pattern is still a shortcoming of the coda normalization method, when it is applied to *P* wave attenuation tomography using passive seismicity.

3. Tomographic Results and Interpretation

3.1. Resolution and Synthetic Testing

We start testing the resolution of the scattering tomography results. We embed a highly scattering volume in a homogeneous medium and use this synthetic model as input for the reconstruction test. This is meant to mimic a strongly scattering contrast under the volcanic cone and its connections with posited deep high-attenuation structures north of it (Figure 4a). The anomalies are all approximately 4 km large in every direction, while the node spacing for the tomography is 2 km. We generate synthetic coda energy and add to these values a Gaussian random error with zero mean and 3 sigma equal to 20% of the data value and apply the inversion scheme.

A highly scattering body below the cone is almost perfectly reconstructed except for some smoothing in the vertical direction (Figure 4a). The scattering factor *g* of the remaining regions is higher on average,

The factor *l* is the length of the segment crossing each block characterized by the velocity *v*(*l*) and quality factor *Q*(*l*), where this last quantity is the parameter modeled in the inversion problem. The factor *G* is dependent on the scattering regime at a constant frequency of 6 Hz and for lapse times larger than 15 s.

The method can be applied to *P* wave tomography if the *P* wave coherent energy is present in the chosen time window and the source radiation pattern effects are sufficiently smoothed at different stations [Yoshimoto *et al.*, 1993; Del Pezzo *et al.*, 2006; Waite *et al.*, 2008]. In the crust, scattering of seismic waves due to small-scale heterogeneities is a major cause of distortion of the *S* wave radiation pattern [Takemura *et al.*, 2009]. In a volcanic region and particularly inside the volcanic edifice, the probability of *P*-to-*S* conversion is much higher than the *P*-to-*P* propagation [Wegler, 2003; De Siena *et al.*, 2013]. Hence, we assume that the early *P*-to-*S* conversion quickly reduces the high-frequency effects of the source radiation pattern at different stations, in analogy to what happens to the *S* wave radiation pattern at crustal scale and in different volcanic areas either with or without topography [Del Pezzo *et al.*, 2006; Takemura *et al.*, 2009; De Siena *et al.*, 2010, 2014]. Nevertheless, the source radiation pattern may still be partially affecting our observations: the unknown persistent effect of the *P* wave source

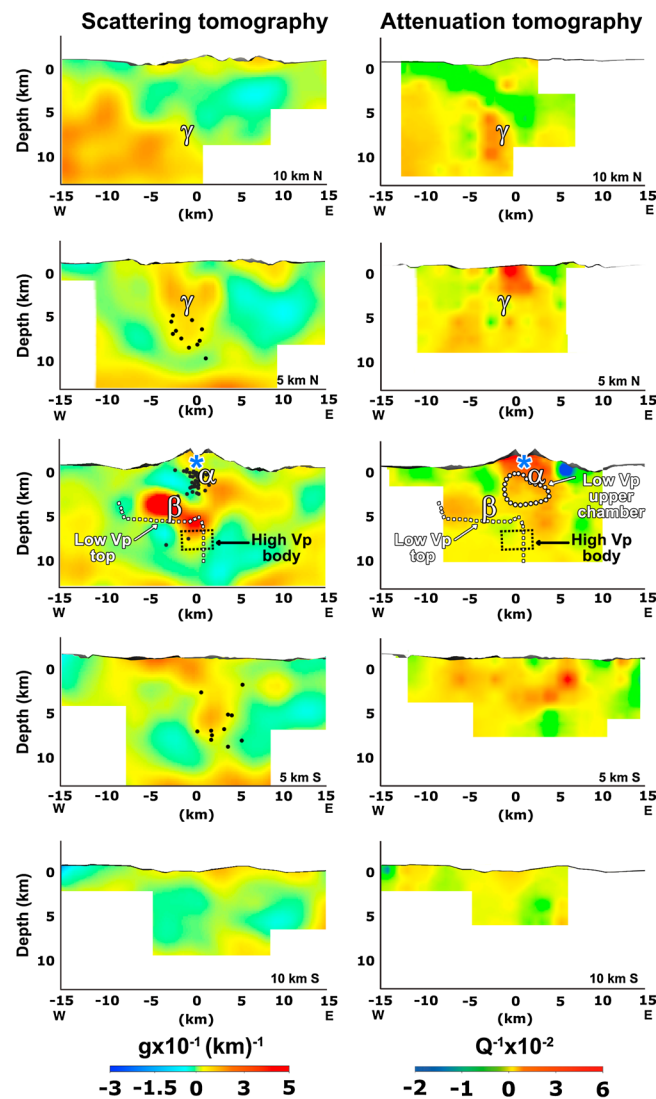


Figure 6. Vertical slices through the 3-D scattering and the P wave attenuation tomographic models are plotted as (left column) scattering coefficient and (right column) total quality factor. Distances are with respect to the central cone. We only show the regions with good recovery of the input in the synthetic tests for the first 13 km of the crust. The seismicity of the period 2005 is overimposed on the three central sections showing the scattering results (black dots). In the scattering tomography model under the cone (Figure 6 third row), we plot the contour of the top of the deeper low-velocity zone, imaged by *Waite and Moran* [2009] (white-dashed line), and the contour of the high-velocity body imaged by *Lees* [1992] (black-dotted line). We add to those the contour of the upper low- V_p magmatic chamber (white-dotted line) on the corresponding attenuation tomography (third row). White-faced bold greek letters label the regions discussed in the text.

being real and not an artifact of errors in data or inversion scheme. Between depths of 0 and 18 km the scattering images are generally reliable except for the volcanic edifice itself where the resolution is affected by our choice of late lapse time (see the SI). Any lateral anomaly not recovered in our tests has been cut from the images.

We also test the resolution of the Q results assuming as input a checkerboard synthetic structure with variable node spacing (Figure 4c) and a reconstruction test of the main anomalies discussed in section 3.2

but we only see secondary effects induced by the inversion in the output (Figure 4b). No spurious high- or low-scattering anomalies are produced by the inversion at depths of 10 to 18 km nor under the edifice or in the surrounding regions.

Because attenuation tomography has resolution only down to 5–6 km depths, we use the scattering tomography results as the main source of information for the interpretation of the seismic structures below 6 km depth. As a second synthetic test we perform a checkerboard test at 4 km node spacing for the scattering tomography images between the surface and 25 km, with the same relative errors added to the reconstruction test input (Figure 5).

The anomalies are generally well-reconstructed except for those inside the cone: we have an average resolution of 2 km in the areas where the primary scattering anomalies appear in our inversion results. Since we considered large lapse times (more than 15 s) coda wave sensitivity results lower in the regions of maximum seismicity, like the cone. Here the inversion of the diffusion equations with respect to diffusivity and intrinsic coefficient would provide better constraints to the physical state of the medium [*Wegler and Lühr*, 2001].

All the tests performed on the scattering tomography results provide an average resolution of 2 to 4 km down to 18 km depth. We are able to reconstruct the characteristics of any high- or low-scattering path connecting upper high-scattering structures with deeper interfaces. This means that we can reliably consider any scattering structure shown in Figures 5–7 as

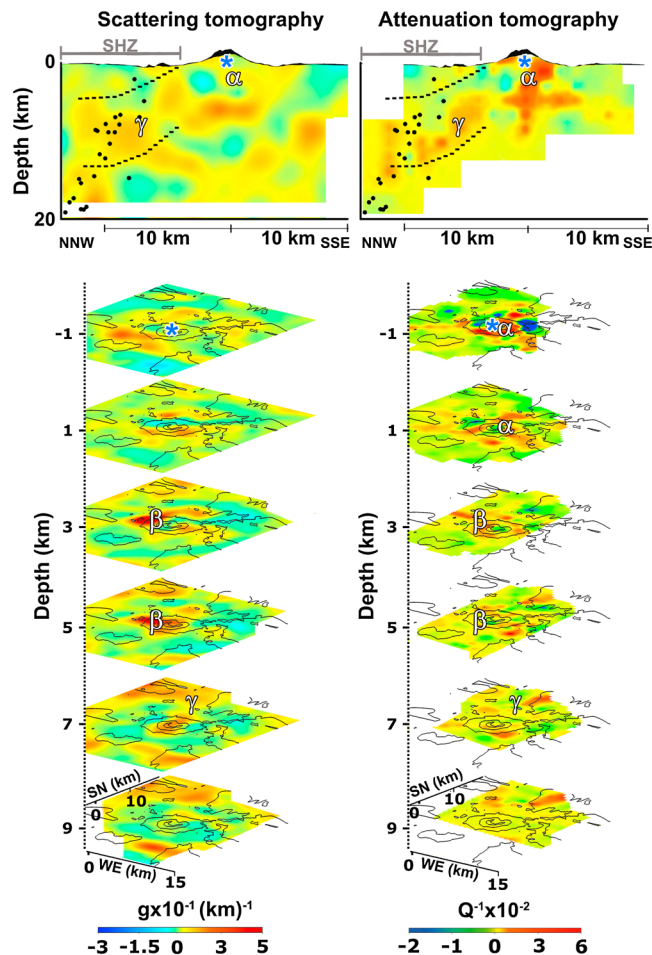


Figure 7. Two vertical slices and five horizontal slices down to the depth of 9 km through the (left) 3-D scattering coefficient and (right) P wave attenuation models. The blue star corresponds to the approximative location of the LP sources, acting during the eruptive period. The vertical sections approximately follow the SHZ. The seismicity recorded along the SHZ in the period 2000–2006 (black dots) is shown on the vertical sections. White-faced bold Greek letters label the regions discussed in the text. High-scattering and high P wave attenuation north of the cone are contoured with a dashed line on the vertical sections and labeled with the letter γ .

3.2. Melt/Fluid Paths, Sediments, and Deeper Feeding Systems

3.2.1. From Surface Down to 6 km Depth Beneath the Volcanic Edifice

Figure 6 shows our results for both the scattering coefficient (g) and the quality factor (Q) 3-D inversions on the same west-to-east vertical sections used to show the velocity results by *Waite and Moran* [2009], with the central section crossing the small dome built during the eruption [*Sherrod et al.*, 2008]. Figure 7 shows the same results on two vertical slices approximately following the SHZ (first row), and on five horizontal tomograms between depths of -1 and 9 km. In the following, we will refer to high-scattering regions when we talk about zones of high g and to high-attenuation regions when we talk about zones of low Q . In Figures 3–8, these volumes are shown in either red, orange, or dark yellow. When we discuss either a high- or low-scattering/attenuation anomaly, we use white-faced Greek letters as label (α , β , γ , and δ).

P wave attenuation tomography shows the highest-attenuation values above 6 km inside the volcanic edifice and upper magmatic chamber (Figure 6, α and white-dotted line). In the same region (red stations, Figure 2) we also record the highest coda energies (SI) as well as very low Q_c (Figure 3, α and δ). In addition,

(Figure 4d). We generate synthetic P -to-coda spectral ratios and add to these a Gaussian random error with zero mean and 3σ (3 times the standard deviation) equal to the 20% of the data value.

The checkerboard test output (Figure 4c) shows a good agreement with the input in the center of the image, while smearing effects are visible in the images at depths greater than 5 km. This test confirms that the maximum P wave resolution can be effectively obtained under the cone, down to a depth of approximately 5–6 km. In the central part of the reconstruction test (Figure 4d), we obtain the best resolution for the volumes characterized by the highest total attenuation between the surface and 6 km depth. Outside of these regions, the images need to be interpreted with caution, due to partial distortion of the solution. In particular, any high-attenuation anomaly north of the cone (e.g., the one we observe along the SHZ at depth of 5 to 18 km (Figure 4d (left))) is strongly smoothed and could not reflect the actual dimension of the attenuating structures. The images rely on the sensitivity of direct waves and give results similar to those obtained by velocity tomography [*Waite and Moran*, 2009] using the coefficients of the resolution matrix. The resolution of the total direct attenuation images strongly decreases below 6 km under the cone, while it slightly improves between 5 and 18 km along the SHZ.

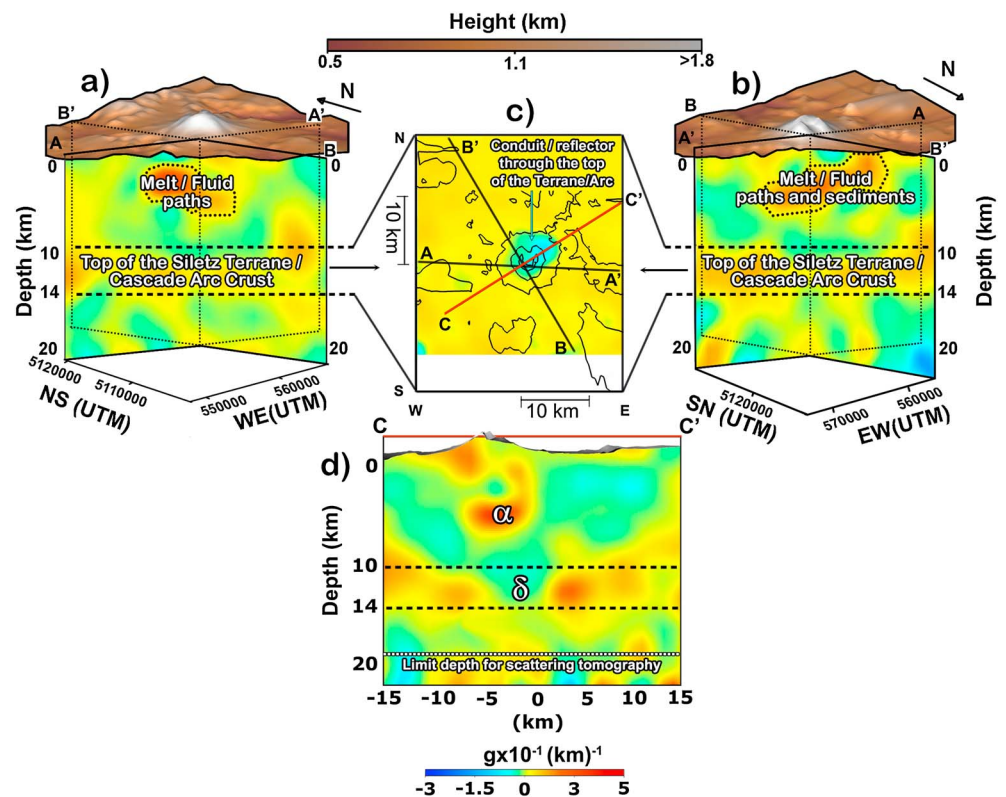


Figure 8. An interpretation of the structures depicted in our results, including a magma/fluid path region, sediments, and a conduit possibly composed of dike-like anomalies. We show the results of the scattering tomography (scattering coefficient g) on three vertical profiles crossing at the cone (AA', BB', and CC'). (a and b) Topography is shown with the brown-grey height scale. Strong scattering is indicated by red colors, weak scattering by blue colors. (c) The directions of these profiles are shown by two black thick lines and one red thick line. The observer is located SW (Figure 8a) and NE (Figure 8b) of the cone, respectively. High-scattering between depths of 2 and 6 km (dotted line) and between depths of 10 and 14 km (thick dashed lines) are indicated. The high-scattering layer between the depths of 10 and 14 km is interpreted as the top of either the Siletz Terrane or the Cascade Arc Crust. The results of the scattering tomography are averaged over depths of 10 and 14 km, and shown in the map of Figure 8c. The low-scattering 4–6 km² hole representing the section of either the magma/fluid-rich conduit or the high-velocity reflector under the northeastern flank of the cone is indicated by a cyan arrow. (d) We show the vertical profile (CC', red line in the map view) crossing both the melt/fluid paths and the hole. White-faced bold Greek letters label the regions discussed in the text.

at stations located on the northern and eastern flanks of the cone, and on the southern part of the SHZ, high attenuation is paired with a significant decrease in energy associated with body waves and coda arrivals, with the appearance of coherent-like scattered phases [De Siena et al., 2013; Margerin, 2013], and with a significant decrease in recorded maximum amplitudes (Figure 3 and S1).

These observations suggest that the volcano and its upper feeding system (including the upper magma chamber depicted by velocity tomography between depths of 1 and 3 km [Lees, 1992; Waite and Moran, 2009]), and particularly the structures under the northern and eastern flanks of the cone, can be seen as a large-scale body producing strong coda absorption as well as scattering power. The presence of a subsurface hydrothermal system active during the eruption, possibly the cause the repeated seismicity [Waite et al., 2008; Matoza and Chouet, 2010], is also a feasible explanation for the attenuation and scattering anomalies, at least in the shallowest portion of the model.

The use of scattering information at large lapse times and the strong heterogeneity of the cone both result in either undersampling of the volumes of highest seismicity (with a consequent loss of resolution, Figures 4 and 5) or instability of the 3-D scattering results in the volcanic edifice. Hence, we do not ensure a good quality for the 3-D scattering results inside the cone (Figure 6, α , see SI for the limits of the 3-D scattering tomography approach). Also, where high seismicity is paired with very high P wave attenuation (Figure 6, α), the breakdown of both the ray approximation and the assumption of homogeneous scattering may strongly

influence ray-dependent techniques and the coda normalization method, respectively [Wegler, 2003; De Siena et al., 2013, 2014].

Coda attenuation is theoretically considered to be equal to intrinsic attenuation within the multiple scattering interpretation of coda waves (our average scattering regime) and after a few mean free times from the source [Sato et al., 2012; Calvet and Margerin, 2013]. As we remarked before, high coda attenuation, with absorption and scattering 1–2 orders of magnitude larger than the rest of the medium, characterizes the northeastern flank of the volcano in a map view (Figure 3, $\alpha - \delta$). We may thus conclude that if the low- Q_c anomaly (Figure 3) is mainly due to absorption (intrinsic loss), it provides a map view of the main feeding structures between depths of 0 and 18 km. This interpretation is to be considered with care and tested with further studies on the lapse time and frequency dependence of Q_c in such a highly heterogeneous region [Calvet and Margerin, 2013].

The 3-D scattering tomography results show that the strongest scatterer in the first 10 km of the crust is located under the cone, between depths of 2 and 6 km (Figures 6, 7, and 8, β), with the seismicity produced during the 2004–2008 eruption located above it (Figure 6, black dots). The anomaly is much larger than the shallow conduit system, which, based on surface observations and geophysical constraints [Pallister et al., 2008; Vallance et al., 2008], is no larger than 0.1–0.2 km in diameter down to depths greater than 1 km. Such a feature is much smaller than the resolution of our model and cannot produce the anomaly at the sampled frequencies (4–8 Hz). The lobed high-scattering body is located at the top of the low-velocity body interpreted as a magmatic chamber below 6 km depth by Waite and Moran [2009] (Figure 6 (third row), β). In the same volumes and by using older seismicity, Lees [1992] show a low-velocity anomaly, extending between depths of 3.5 and 6 km, which lies at the top of a high-velocity anomaly (6–9 km deep). The upper low-velocity anomaly is also spatially correlated with the high-scattering body.

Due to the lateral extension of the anomaly, one likely candidate to produce it is the edifice itself, which is highly heterogeneous and composed of a series of older fractured dacite domes and lava flows of andesite and basaltic andesite, all of which could produce high-scattering contrasts [Nishigami, 2000; Wegler, 2003; Tramelli et al., 2006]. However, the depth of this anomaly is much greater than where we expect such effects to appear. In our interpretation, the cone remains a feasible candidate only in the regions also characterized by high P wave attenuation, down to 2 km depth.

One feasible interpretation is that the high-scattering anomaly, located below the new lava dome and possibly producing strong coherent-like scattering in regions above and immediately surrounding the body [Margerin, 2013], represents a low-velocity magma/fluid chamber. Due to the difficulty associated to the interpretation of scattering images in such a complex region, we cannot exclude that the anomaly is a direct image of a magma chamber. The high-scattering contrast may therefore be induced by the high-velocity anomaly (Figure 7, black-dashed line), interpreted as a plug by Lees [1992], and whose dip is similar to the shift in the feeding system visible below 10 km, and discussed in the following sections.

In our interpretation, however, this anomaly reveals the pathways of fluid/melt (Figures 6, 7a, and 7b) coming from depth and feeding the eruption more than the actual location of a magma chamber. Similar pathways have been revealed by the 3-D scattering tomography of Asano et al. [2004] at the top of an extended low-velocity anomaly [Nakajima and Hasegawa, 2003], this last being a fluid-filled zone connected with both volcanic centers and active faults. Figure 7 (third row, left, β , white-dashed line) shows that the high-scattering anomaly is mainly located at the top of a low-velocity volume interpreted as a magma/fluid chamber by Waite and Moran [2009]. We infer, therefore, that this is the main path followed by either melt or fluid between depths of 2 and 5 km, feeding the eruption and the lava-dome growth.

3.2.2. St. Helens Seismic Zone

The only high-scattering and high-attenuation anomaly connecting the melt/fluid high-scattering anomaly under the MSH cone with deeper structures as far as 15 km north of the cone is visible between 0 and 10 km depth (Figure 7, vertical tomograms, inside the dashed lines, γ). Scattering and attenuation in these volumes are lower than beneath the MSH cone (Figures 6 and 7, see also Figure 3, γ). The anomalies are spatially correlated with a low P wave velocity north-south trending trough [Moran et al., 1999] as well as with a strong lowering of the seismic amplitudes (a_m , Figure 2). North of the cone (e.g., Figure 6, panel 10 km N, γ), a high-attenuation and high-scattering anomaly develops west of the SHZ.

An interpretation of the volumes containing the SHZ must be done with caution. The SHZ volumes are affected by strong smoothing in the P wave attenuation images and by the only instability observed in the 3-D scattering tomography results (see the SI section S3). Also, guided waves may rise in the low-velocity SHZ fault zone and cracked sediment-filled surroundings [Li and Vidale, 1996]. These quasi-isotropic waves show a spectral peak above 3 Hz, which decays sharply with distance from the SHZ, and an opposite trend at high frequencies (8–15 Hz [Li et al., 1994; Li and Vidale, 1996]). The effects induced by these waves are to increase coda wave intensities and decrease of direct wave intensities: this translates into an increase of both scattering and attenuation along the fault [Nishigami, 2000; De Siena et al., 2014].

The attenuation and scattering results are consistent with the interpretation of Moran et al. [1999], who infer the presence of Tertiary marine sediments that fill the SHZ fault region and strongly attenuate any wavefield crossing them. As shown by Nishigami [2000], faulting is also a major factor for high scattering. Although an interpretation in terms of relative intensity of high-scattering anomaly must be done with care, we remark the lower scattering power of these structures with respect to the regions where the eruption takes place. If we assume as valid the study of Margerin [2013] on near-station resonance effects induced by a low-velocity body, this difference could be attributed to the difference in scattering potential between a cracked medium filled with sediments and the low-velocity one filled with either melt or fluid.

As far as 15 km north-north-west of Mount St. Helens a high-attenuation and high-scattering anomaly fits with the high conductance measurements of Egbert and Booker [1993], which may constitute either the stratification of sediments at depth or (due to the very high-scattering power) a fluid-filled medium. On the other hand, these are the volumes of highest instability for the 2-D Q_c and the 3-D scattering tomography. A stability test, performed by excluding the seismicity before the eruption from those inversions, shows that the anomalies under the northernmost extension of the SHZ almost disappear: if this is due to the smaller sampling of the fault region, we cannot exclude that the anomalies are inversion artifacts.

3.2.3. From 10 km Down to 18 km Depth

Between depths of 10 and 20 km, no reliable information can be retrieved from the 3-D P wave attenuation tomography under the cone (Figure 4). In the scattering images, no vertical path of melt/fluids is visible as a unique vertical conduit of high-scattering power connecting the shallow high-scattering anomaly with high-scattering structures at larger depths (down to a depth of 18 km, Figures 8a and 8b). At a depth of around 10 km, however, a thin (2 to 4 km wide) strong scattering layer extends under the whole volcanic area (Figures 8a and 8b).

We relate the presence of the high-scattering anomalies in this depth range to the boundary between upper and middle crust, and, more specifically, to the top of either the accreted Siletz terrane (a fragment of crustal material formed on, or broken off from, one tectonic plate) or older Cascade arc crust [Parsons et al., 2005]. This would be an area of strong horizontal and vertical contrast in material properties, which would lend itself to scattering in the entire region (Figure 8c) and would explain the strong scattering contrasts between volumes west and east of the SHZ (Figures 6 and 7, 10 km north of the cone).

Inside the high-scattering layer starting at ≈ 10 km depth, the most interesting anomaly we resolve is a very low scattering anomaly under the northeastern flank of the volcanic cone (Figure 8c, δ). This 4–6 km² “hole” is centered 2 km north-east with respect to the shallower high-scattering and high-attenuation anomalies imaged at depths of 2 to 6 km directly beneath MSH cone. The scattering images as well as the vertical increase in total attenuation between depth of -1 and 6 km all suggest the presence of a conduit system feeding melt/fluid materials to the eruption. The northeastern shift of the hole at depths of 10 to 14 km (Figure 8c) suggests a northeastern shift of such conduit with respect to the shallow magmatic chambers depicted by Waite and Moran [2009]. The anomaly correlates well both with the location of the upper part of a highly conductive conduit [Hill et al., 2009] and with the eastward dipping direction of the feeding system, which was hypothesized by Lees [1992] (Figure 1).

The conductive vertical conduit imaged by Hill et al. [2009] ends between depths of 10 and 15 km in a vast sill extending toward east, interpreted by the authors as the top of the Southern Washington Cascades Conductor [Egbert and Booker, 1993]. The top of the deep resistive anomaly is in good correlation with the almost horizontal high-scattering contrast between depths of 10 and 14 km in the tomograms of Figures 8a and 8b. However, the 3-D scattering results show no evidence of any vast magma-filled sill (at least larger than 4–6 km², Figure 8, δ) extending only toward east between depths of 10 and 18 km. The extension

of the high-scattering layer is too large in the western and southern directions to be induced by a unique melt/fluid sill located east of the cone.

We cannot exclude that the top of the highly conductive anomaly, interpreted by *Hill et al.* [2009] as the Southern Washington Cascades Conductor, could be located at depths larger than 18 km. As shown by *Hill et al.* [2009], the locations of earthquakes deeper than 11 km at the time of the 1980 eruption [*Scandone and Malone*, 1985] are concentrated only near the western margin of the midcrustal conductor, suggesting a large aseismic zone of partial melt East of this boundary (Figure 1). However, in our interpretation, the interaction of the Siletz Terrane with the Cascade Arc crust [*Parsons et al.*, 2005] has a major role in producing the deep strong scattering contrast in our images below 10 km (Figures 8a and 8b): this interaction (Figure 1) presents a small eastward slope compatible with the seismicity recorded in 1980 at depths greater than 11 km [*Parsons et al.*, 2005; *Scandone and Malone*, 1985]. We assume that scattering tomography may produce images having higher depth resolution with respect to electromagnetic tomography in this depth range: this is mainly an effect induced by the presence of deep seismic sources, which may better sample the bottom part of volcanic structures with different seismic characteristics.

The northeastern shift of the deep feeding system (Figure 8, δ) is compatible with the spatial characteristics of most of the events recorded between 1996 and 1999 at depths greater than 5 km. These vents occur on a NNE-SSW striking steeply dipping fault with slip consistent with magma being periodically injected into a truncated dike on the northwest side of this fault [*Musumeci et al.*, 2002]. Also, the comparison of petrological studies done by *Pallister et al.* [2008] with rock and gas samples related either to the 1980–1986 or to the Goat Rocks (A.D. 1800–1857) eruptive cycles suggests temporal changes in the upper feeding system of the volcano.

In our preferred interpretation, the hole is induced by a network of interconnected water-rich melt fractions, whose individual size is smaller than our resolution [*Hill et al.*, 2009]. The dimension of each fraction could be too small to be detected at 6 Hz, but their total absorption effect would still modify the decay rate of the coda, causing the decrease of the scattering coefficient mainly due to intrinsic mechanisms. Except for the shift in the conduit system, this mechanism is similar to the one proposed for the eruption in 1980 [*Heliker*, 1995; *Costa et al.*, 2007; *Scandone et al.*, 2007]. This interpretation is also supported by the location of the low- Q_c anomaly, if we assume that large lapse time coda Q is a good indicator of intrinsic attenuation (Figure 3, δ). If the low-scattering hole at depths of 10 to 14 km marks the section of the conduit feeding the chamber in the strong scattering contrast, we infer that melt and magmatic fluids may directly come from the subducting structures deeper than 18 km in the Cascadia subduction zone [*Defant and Kepezhinskas*, 2001; *Wells and Simpson*, 2001].

On the other hand, deformation modeling images a 2004–2008 magmatic system extending straight down from the surface to depths greater than 10 km [*Mastin et al.*, 2008], while *Hill et al.* [2009] obtain a vertical conductive high-resistivity anomaly between depths of 2 and 10 km. All these considered, we remark the spatial correlation between the scattering tomography images (depths of 6 and 14 km, Figure 8c) and the high-velocity body dipping eastward (Figure 1), obtained by *Lees* [1992], and interpreted as a plug for volcanic eruptions. This plug would actually be able to break the high-scattering layer at 10–14 km depth (Figure 8, δ), producing the low-scattering anomaly, and its top could induce the high-scattering contrast at 6–7 km depth (Figure 8, β). If we accept this interpretation, it is necessary to understand the feasibility and volcanological consequences of the presence of this massive body under an erupting volcano as well as why we are not able to depict its high-scattering sides.

The 4–6 km² hole evident in the high-scattering boundary between depths of 10 and 14 km is clearly related to the feeding system of the volcano. The separation and mapping of intrinsic and scattering attenuation may solve this bias and strongly enhance our interpretation, even if, especially in heterogeneous media, scattering anomalies have a complex signature, which is hard to attribute to seismic and volcanological structures [*Chung et al.*, 2009; *Sato et al.*, 2012; *Margerin*, 2013; *Calvet and Margerin*, 2013; *Mayor et al.*, 2014].

4. Conclusions

Q_c mapping, P wave attenuation tomography, and scattering tomography used together on seismic data recorded in the period 2000–2006 provide images of the deep structures feeding the MSH volcanic system down to around 18 km depth. We interpret the results to be associated with the MSH plumbing system.

A high coda attenuation, high P attenuation, and high-scattering anomaly beneath the cone shows the location of the magma/fluid zone feeding the volcano and producing the seismicity inside the cone. The region is not connected by any continuous resolvable vertical highly scattering structure to depths greater than 7 km. A north-trending high coda attenuation, high P attenuation, and high-scattering anomaly correlated with a low P wave velocity north-south trending trough as well as with a strong lowering of the seismic amplitudes is inferred to be due to the cracked SHZ fault structures, possibly filled by Tertiary marine sediments down to 10 km depth.

A highly scattering layer between depths of 10 and 14 km extends under the entire region. We infer that this scattering contrast shows the top of either the accreted Siletz terrane (a fragment of crustal material formed on, or broken off from, one tectonic plate) or the older Cascade arc crust, interacting in this depth range. Finally, after considering all the geophysical and geological constraints, we prefer to interpret a low-scattering 4–6 km² hole centered 2 km north-east with respect to the shallower magma chamber in this highly scattering layer as the section of the conduit system feeding deeper melt/fluid materials to the eruption. Nevertheless, both the separation and mapping of intrinsic and scattering attenuation from coda waveforms and the joint inversion of scattering parameters with different geophysical data would strongly improve our interpretations of this as well as of the previously discussed structures.

The exploitation of full-waveform information is still an unexplored field in volcano tomography. The three techniques proposed here show that the addition of scattering and attenuation tomography information to velocity tomography provides reliable images both near to and far from the theoretical direct ray between source and station. This represents a critical improvement to current travel time volcano tomography images. We infer that the future for imaging volcanic structures stands in the adjustment of full-waveform tomography techniques to highly scattering media.

Acknowledgments

We thank Edoardo Del Pezzo, Ludovic Margerin, Christoph Sens-Schönfelder, Michael Becken, David Hill, Matt Haney, Willie Scott, Alicia Hotovec-Ellis, Jonathan Lees, and two anonymous reviewers for their suggestions and critical reviews. Steve Hicks, Carina Häger, and Laura Schmidt helped in the data processing. The facilities of the IRIS Data Management System, and specifically the IRIS Data Management Center, were used for access to waveform and metadata required in this study and provided by the Cascades Volcano Observatory - USGS. The MuRAT code with two sample applications is freely available at http://earth.uni-muenster.de/~ldesi_01/publications/publications.html under free license. The methods for the 2-D and 3-D scattering tomographies are based on the ones described in *Tramelli et al.* [2006] and *Calvet et al.* [2013]. Supporting information accompanies this paper. Correspondence and requests for materials should be addressed to Luca De Siena.

References

- Aki, K. (1980), Attenuation of shear-waves in the lithosphere for frequencies from 0.05 to 25 Hz, *Phys. Earth Planet. Inter.*, *21*, 50–60.
- Aki, K., and B. Chouet (1975), Origin of coda waves: Source, attenuation, and scattering effects, *J. Geophys. Res.*, *80*, 3322–3342.
- Asano, Y., and A. Hasegawa (2004), Imaging the fault zones of the 2000 western Tottori earthquake by a new inversion method to estimate three-dimensional distribution of the scattering coefficient, *J. Geophys. Res.*, *109*, B06306, doi:10.1029/2003JB002761.
- Asano, Y., K. Obara, J. Nakajima, and A. Hasegawa (2004), Inhomogeneous crustal structure beneath northern Miyagi prefecture, northeastern Japan, imaged by coda envelope inversion: Implication for fluid distribution, *Geophys. Res. Lett.*, *31*(24), L24615, doi:10.1029/2004GL021261.
- Block, L. V. (1991), Joint hypocenter-velocity inversion of local earthquake arrival time data in two geothermal regions, PhD dissertation, Mass. Inst. of Technol., Cambridge, U. K.
- Calvet, M., and L. Margerin (2013), Lapse-time dependence of coda Q: Anisotropic multiple-scattering models and application to the Pyrenees, *Bull. Seismol. Soc. Am.*, *103*(3), 1993–2010.
- Calvet, M., M. Sylvander, L. Margerin, and A. Villaseñor (2013), Spatial variations of seismic attenuation and heterogeneity in the Pyrenees: Coda Q and peak delay time analysis, *Tectonophysics*, *608*, 428–439.
- Chung, T. W., J. M. Lees, K. Yoshimoto, E. Fujita, and M. Ukawa (2009), Intrinsic and scattering attenuation of the Mt Fuji Region, Japan, *Geophys. J. Int.*, *177*(3), 1366–1382.
- Costa, A., O. Melnik, R. S. J. Sparks, and B. Voight (2007), Control of magma flow in dykes on cyclic lava dome extrusion, *Geophys. Res. Lett.*, *34*(2), L02303, doi:10.1029/2006GL027466.
- Defant, M. J., and P. Kepezhinskas (2001), Evidence suggests slab melting in arc magmas, *Eos Trans. AGU*, *82*(6), 65–69.
- Del Pezzo, E., F. Bianco, L. De Siena, and A. Zollo (2006), Small scale shallow attenuation structure at Mt. Vesuvius, *Phys. Earth Planet. Inter.*, *157*, 257–268.
- De Siena, L., E. Del Pezzo, and F. Bianco (2010), Campi Flegrei seismic attenuation image: Evidences of gas reservoirs, hydrothermal basins and feeding systems, *J. Geophys. Res.*, *115*, B09312, doi:10.1029/2009JB006938.
- De Siena, L., E. Del Pezzo, C. Thomas, A. Curtis, and L. Margerin (2013), Seismic energy envelopes in volcanic media: In need of boundary conditions, *Geophys. J. Int.*, *192*(1), 326–345.
- De Siena, L., C. Thomas, and R. Aster (2014), Multi-scale reasonable attenuation tomography analysis (MuRAT): An imaging algorithm designed for volcanic regions, *J. Volcanol. Geotherm. Res.*, *277*, 22–35.
- Egbert, G. D., and J. R. Booker (1993), Imaging crustal structure in southwestern Washington with small magnetometer arrays, *J. Geophys. Res.*, *98*, 15,967–15,985.
- Fehler, M. C., P. Roberts, and T. Fairbanks (1988), A temporal change in coda wave attenuation observed during an eruption of Mount St. Helens, *J. Geophys. Res.*, *93*, 4367–4373.
- Heliker, C. (1995), Inclusions in Mount St. Helens dacite erupted from 1980 through 1983, *J. Volcanol. Geotherm. Res.*, *66*(1), 115–135.
- Hill, G., T. Caldwell, W. Heise, D. Chertkoff, H. Bibby, M. Burgess, J. Cull, and R. Cas (2009), Distribution of melt beneath Mount St Helens and Mount Adams inferred from magnetotelluric data, *Nat. Geosci.*, *2*(11), 785–789.
- Lees, J. (1992), The magma system of Mount St. Helens: Non-linear high-resolution P-wave tomography, *J. Volcanol. Geotherm. Res.*, *53*(1), 103–116.
- Lees, J. M., and R. S. Crosson (1989), Tomographic inversion for three-dimensional velocity structure at Mount St. Helens using earthquake data, *J. Geophys. Res.*, *94*, 5716–5728.
- Li, Y., and J. E. Vidale (1996), Low-velocity fault-zone guided waves: Numerical investigations of trapping efficiency, *Bull. Seismol. Soc. Am.*, *86*(2), 371–378.

- Li, Y. G., K. Aki, D. Adams, A. Hasemi, and W. H. K. Lee (1994), Seismic guided waves trapped in the fault zone of the Landers, California, earthquake of 1992, *J. Geophys. Res.*, *99*(B6), 11,705–11,722.
- Margerin, L. (2013), Diffusion approximation with polarization and resonance effects for the modelling of seismic waves in strongly scattering small-scale media, *Geophys. J. Int.*, *192*(1), 326–345.
- Margerin, L., and G. Nolet (2003), Multiple scattering of high-frequency seismic waves in the deep Earth: Modeling and numerical examples, *J. Geophys. Res.*, *108*(B5), 2234–2249, doi:10.1029/2002JB001974.
- Mastin, L. G., E. Roeloffs, N. M. Beeler, and J. E. Quick (2008), Constraints on the size, overpressure, and volatile content of the Mount St. Helens magma system from geodetic and dome-growth measurements during the 2004–2006 eruption, in *A Volcano Rekindled: The Renewed Eruption of Mount St. Helens, 2004–2006*, edited by D. R. Sherrod, W. E. Scott, and P. H. Stauffer, *U.S. Geol. Surv. Prof. Pap.*, *1750*, 461–488.
- Matoza, R. S., and B. A. Chouet (2010), Subevents of long-period seismicity: Implications for hydrothermal dynamics during the 2004–2008 eruption of Mount St. Helens, *J. Geophys. Res.*, *115*, B12206, doi:10.1029/2010JB007839.
- Matsumoto, S., K. Obara, and A. Hasegawa (1998), Imaging P-wave scatterer distribution in the focal area of the 1995 M7.3 Hyogo-ken Nanbu (Kobe) Earthquake, *Geophys. Res. Lett.*, *25*(9), 1439–1442.
- Mayor, J., L. Margerin, and M. Calvet (2014), Sensitivity of coda waves to spatial variations of absorption and scattering: Radiative transfer theory and 2-D examples, *Geophys. J. Int.*, *197*, 1117–1137.
- Moran, S. C., J. M. Lees, and S. Malone (1999), P-wave crustal velocity structure in the greater Mount Rainier area from local earthquake tomography, *J. Geophys. Res.*, *104*(B5), 10,775–10,786.
- Musumeci, C., S. Gresta, and S. D. Malone (2002), Magma system recharge of Mount St. Helens from precise relative hypocenter location of microearthquakes, *J. Geophys. Res.*, *107*(B10), 2264, doi:10.1029/2001JB000629.
- Nakajima, J., and A. Hasegawa (2003), Tomographic imaging of seismic velocity structure in and around the Onikobe volcanic area, northeastern Japan: Implications for fluid distribution, *J. Volcanol. Geotherm. Res.*, *127*, 1–18.
- Nishigami, K. (1991), A new inversion method of coda waveforms to determine spatial distribution of coda scatterers in the crust and uppermost mantle, *Geophys. Res. Lett.*, *12*(18), 2225–2228.
- Nishigami, K. (2000), Deep crustal heterogeneity along and around the San Andreas fault system in central California and its relation to the segmentation, *J. Geophys. Res.*, *105*, 7983–7998.
- Nishigami, K. (2006), Crustal heterogeneity in the source region of the 2004 Mid Niigata Prefecture earthquake: Inversion analysis of coda envelopes, *Pure Appl. Geophys.*, *163*, 601–616.
- Pallister, J. S., R. P. Hoblitt, D. R. Crandell, and D. R. Mullineaux (1992), Mount St. Helens a decade after the 1980 eruptions: Magmatic models, chemical cycles, and a revised hazards assessment, *Bull. Volcanol.*, *54*(2), 126–146.
- Pallister, J. S., C. R. Thornber, K. V. Cashman, M. A. Clyne, H. A. Lowers, C. W. Mandeville, I. K. Brownfield, and G. P. Meeker (2008), Petrology of the 2004–2006 Mount St. Helens lava dome—Implications for magmatic plumbing and eruption triggering, in *A Volcano Rekindled: The Renewed Eruption of Mount St. Helens, 2004–2006*, edited by D. R. Sherrod, W. E. Scott, and P. H. Stauffer, *U.S. Geol. Surv. Prof. Pap.*, *1750*, 647–702.
- Parsiegla, N., and U. Wegler (2008), Modelling of seismic energy transport at volcanoes with real topography and complex propagation medium, *J. Volcanol. Geotherm. Res.*, *171*, 229–236.
- Parsons, T., et al. (2005), Crustal structure of the Cascadia fore arc of Washington, in *Earthquake Hazards of the Pacific Northwest Coastal and Marine Regions*, edited by R. Kayen, *U.S. Geol. Surv. Prof. Pap.*, *1661-D*.
- Sato, H., M. C. Fehler, and T. Maeda (2012), *Seismic Wave Propagation and Scattering in the Heterogeneous Earth*, 2nd ed., 494 pp., Springer, New York.
- Scandone, R., and S. D. Malone (1985), Magma supply, magma discharge and readjustment of the feeding system of Mount St. Helens during 1980, *J. Volcanol. Geotherm. Res.*, *23*(3), 239–262.
- Scandone, R., K. V. Cashman, and S. D. Malone (2007), Magma supply, magma ascent and the style of volcanic eruptions, *Earth Planet. Sci. Lett.*, *253*(3), 513–529.
- Sherrod, D. R., W. E. Scott, and P. H. Stauffer (Eds.) (2008), *A Volcano Rekindled: The Renewed Eruption of Mount St. Helens, 2004–2006*, *U.S. Geol. Surv. Prof. Pap.*, *1750*.
- Takemura, S., T. Furumura, and T. Saito (2009), Distortion of the apparent S-wave radiation pattern in the high-frequency wavefield: Tottori-Ken Seibu, Japan, earthquake of 2000, *Geophys. J. Int.*, *178*(2), 950–961.
- Tramelli, A., E. Del Pezzo, F. Bianco, and E. Boschi (2006), 3D scattering image of the Campi Flegrei caldera (Southern Italy): New hints on the position of the old caldera rim, *Phys. Earth Planet. Inter.*, *155*, 269–280.
- Tramelli, A., E. Del Pezzo, and M. Fehler (2009), 3D scattering image of Mt. Vesuvius, *Bull. Seismol. Soc. Am.*, *99*(3), 1962–1972.
- Tusa, G., S. D. Malone, E. Giampiccolo, S. Gresta, and C. Musumeci (2004), Attenuation of short-period P waves at Mount St. Helens, *Bull. Seismol. Soc. Am.*, *94*(4), 1441–1455, doi:10.1785/012003040.
- Vallance, J. W., D. J. Schneider, and S. P. Schilling (2008), Growth of the 2004–2006 lava-dome complex at Mount St. Helens, Washington, in *A Volcano Rekindled: The Renewed Eruption of Mount St. Helens, 2004–2006*, edited by D. R. Sherrod, W. E. Scott, and P. H. Stauffer, *U.S. Geol. Surv. Prof. Pap.*, *1750*, 169–208.
- Waite, G., and S. Moran (2009), Vp Structure of Mount St. Helens, Washington, USA, imaged with local earthquake tomography, *J. Volcanol. Geotherm. Res.*, *182*, 113–122.
- Waite, G., B. A. Chouet, and P. B. Dawson (2008), Eruption dynamics at Mount St. Helens imaged from broadband seismic waveforms: Interaction of the shallow magmatic and hydrothermal systems, *J. Geophys. Res.*, *113*, B02305, doi:10.1029/2007JB005259.
- Wegler, U. (2003), Analysis of multiple scattering at Vesuvius Volcano, Italy, using data of the TomoVes active seismic experiment, *J. Volcanol. Geotherm. Res.*, *128*, 45–63.
- Wegler, U., and B. G. Lühr (2001), Scattering behaviour at Merapi Volcano (Java) revealed from an active seismic experiment, *Geophys. J. Int.*, *145*, 579–592.
- Wells, R. E., and R. W. Simpson (2001), Northward migration of the Cascadia forearc in the northwestern US and implications for subduction deformation, *Earth Planets Space*, *53*(4), 275–284.
- Yamamoto, M., and H. Sato (2010), Multiple scattering and mode conversion revealed by an active seismic experiment at Asama volcano, Japan, *J. Geophys. Res.*, *115*, B07304, doi:10.1029/2009JB007109.
- Yoshimoto, K., H. Sato, and M. Ohtake (1993), Frequency-dependent attenuation of P and S waves in the Kanto area, Japan, based on the coda-normalization method, *Geophys. J. Int.*, *114*, 165–174.